
Microstructure and mechanical properties of Ti basic bionic gradient heterogeneous alloy prepared by multi-wire arc additive manufacturing

P.F. Jiang^a, X.R. Li^a, X.M. Zong^{b,*}, X.B. Wang^c, Z.K. Chen^b, C.Z. Liu^d, N.K. Gao^a, Z.H. Zhang^{a,*}

^a Key Laboratory of Bionic Engineering, (Ministry of Education) and College of Biological and Agricultural Engineering, Jilin University, 5988 Renmin Street, Changchun 130025, China

^b State Key Laboratory of Intelligent Manufacturing of Advanced Construction Machinery, Xuzhou 221004, China

^c Key Laboratory for Liquid-Solid Structural Evolution and Processing of Materials (Ministry of Education), Shandong University, Jingshi Road 17923, Jinan 250061, China

^d Institute of Orthopaedic & Musculoskeletal Science, University College London, Royal National Orthopaedic Hospital, Stanmore, London HA7 4LP, UK

ABSTRACT

Inspired by biological gradient structure, Ti basic gradient heterogeneous alloy component from TC11 alloy to TC4 alloy was fabricated by multi-wire arc additive manufacturing (MWAAM). The chemical mixing, phase and microstructure evolution, microhardness distribution and tensile property of Ti basic gradient heterogeneous alloy were investigated through EDS, XRD, SEM, hardness tester and tensile tester. The results indicated that the alloy elements formed a long-distance gradient concentration distribution during the transition between two different titanium alloys due to dilution, remelting, and convective mixing in the molten pool. The intensity of diffraction peaks of Ti basic gradient heterogeneous alloy in the gradient region had no obvious change. The microstructure of MWAAM Ti basic gradient heterogeneous alloy was mainly consisted of lamellar α_p , acicular α_s , equiaxed α_s and β matrix. Different morphology of the α_s phase was mainly attributed to the wetting state of the second solid phase and grain boundary. In addition, the microstructure of α phase in Ti basic gradient heterogeneous alloy was significantly changed by the gradient distribution of alloy composition. The gradient heterogeneous alloy component manufactured in this work had high bonding strength. The average UTS of MWAAM Ti basic gradient heterogeneous alloy was 793.14 MPa, which was close to MWAAM TC4 alloy and reached approximately 85% of MWAAM TC11 alloy.

1. Introduction

Wire arc additive manufacturing technology (WAAM) is a technology that uses arc as heat source to deposit materials layer by layer to directly manufacture large metal components [1,2]. It is widely concerned because of its high deposition rate, high material utilization, and relatively low production and equipment costs [3]. Since the development of WAAM technology, it is gradually deepening from the aspects of design, manufacturing, materials, equipment, various processes of process technology, and many fields of industrial application. At present, most of the molding materials involved in WAAM, especially the metal material system, are only manufactured for a single homogeneous material [4–6]. However, in the fields of national defense and military, aerospace, biomedicine,

green energy and other industries, there is little research on the manufacturing additive technology of heterogeneous metal with significant application value and innovative advantages.

For aerospace components, in order to meet the needs of different components in different service environments, combining different materials into a single component is an effective solution to expand the overall functional characteristics [7,8]. However, there are many problems in the connection of heterogeneous metal components, such as mismatched material combinations, poor interface bonding, and difficult to control performance [9–12]. Therefore, it is necessary to optimize the connection structure of heterogeneous metal materials.

Natural biological gradient structures in nature provide the most perfect solution for the design of heterogeneous metal functional structures [13]. For example, the bones and teeth of animals and the bamboo in plants have evolved and optimized for hundreds of millions of years. They have already developed into heterogeneous objects composed of a variety of functional materials. Their material composition and structural characteristics have gradient differences

* Corresponding authors.

E-mail addresses: 13776580177@139.com (X.M. Zong), zhzh@jlu.edu.cn (Z.H. Zhang).

Table 1

The nominal chemical compositions of the TC11 and TC4 alloy wires.

	Al	Mo	Zr	V	Si	Fe	C	N	O	Ti
TC11	6.52	3.39	1.74	-	0.30	0.07	0.01	0.01	0.11	Bal.
TC4	6.20	-	-	4.02	-	0.02	0.01	0.01	0.09	Bal.

Table 2

The optimized MWAAM process parameters about this experiment.

	TC11	TC4
Arc current (A)	150	144
Average voltage (V)	14.0	14.0
Wire feed velocity (cm/min)	200	200
Hot-wire current (A)	120	120
Moving speed (mm/min)	360	360
Layer thickness (mm)	1.5	1.5
Shielding gas flow rate (L/min)	20	20

in spatial distribution, which has the outstanding advantage of multi-functional optimization integration [14,15]. With the help of multi-dimensional and multi-scale bionic gradient structure design and additive manufacturing technology, the integrated manufacturing of functional modular heterogeneous metal parts can be realized.

Titanium alloy plays an important role and strategic position in aircraft structure due to its excellent mechanical and physical properties [16–20]. Recently, the development and application of dual titanium heterogeneous alloys components also have been attracted more and more attention by researchers. Chen et al. [7] had deposited TC11 alloy samples on TC17 substrate by WAAM, and studied the effects of different annealing temperatures on the microstructure and properties of TC11-TC17 double alloy samples. They found that the hardness of TC17 increased slightly after annealing at 560 °C, but the tensile properties did not change significantly. Moreover, the ductility was improved due to the wide α phase and uniform microstructure after annealing at 700 °C and 800 °C. Kennedy et al. [15] reported the effect of alloy composition on phase microstructure of the two high-performance dissimilar titanium alloys (Ti-5Al-5V-5Mo-3Cr and Ti-6Al-4V) tailored components by WAAM. The results showed that the change of alloy composition had almost no obvious effect on the β -grain structure, but had a significant effect on the transformation microstructure of the α phase. Liu et al. [21] investigated the mechanical properties of laser additive manufacturing TA15-Ti2AlNb bimetallic components. The TA15-Ti2AlNb bimetallic structures presented excellent tensile properties in this work, and the average tensile strength was 1025 MPa and

elongation was 7.3%. Wang et al. [22] prepared a material transition from TA15 to TC11 by WAAM. The results showed that the strength at the interface was higher than the longitudinal strength of TA15, and the transverse elongation at the interface was higher than TA15 and TC11. Although there have been some reports on the fabrication of dual titanium heterostructures components with additive manufacturing, the research on the microstructure and functional properties of the transition region is still lacking.

In this study, a large size of Ti basic bionic gradient heterogeneous alloy component from Ti-6.5Al-3.5Mo-1.5Zr-0.3Si (TC11) to Ti6Al4V (TC4) was designed by multi-wire arc additive manufacturing (MWAAM) technology, which aims at the practical application of compressor blades and discs of aeroengines in aerospace industry [23]. The distribution of elements, phase and microstructure evolution, mechanical properties were experimentally characterized to try to establish the relationship of process-micro-structure-property in TC11-TC4 bionic gradient heterogeneous alloy component. This knowledge can be used to help control the range and performance of the transition region in the Ti basic gradient heterogeneous alloy structural parts. In addition, the research in this paper provides a certain theoretical basis for the MWAAM large-scale gradient heterogeneous alloy components.

2. Material and methods

2.1. Multi-wire arc additive manufacturing

In this experiment, TC11 and TC4 alloy wires with a diameter of 1.2 mm were used as raw materials. The nominal chemical compositions of the TC11 and TC4 alloy wires is shown in Table 1. The MWAAM system consists of a 6-axis ABB robot arm with a IRC5 controller, a shielding gas unit and wire feeders. The tungsten inert gas (TIG) torch is installed on the ABB robot which can move upwards and downwards. The resistance heat power sources were used to greatly reduce heat from the arc. The MWAAM environment was in the enclosed atmosphere with 99.99% purity argon. The more detail of other fundamental modules of the MWAAM can be found in previous work [24]. The Ti basic gradient heterogeneous alloy component (about 200 mm long, 60 mm wide and 120 mm high) from TC11 to TC4 was deposited on TC11 substrate by MWAAM. The optimized MWAAM process parameters were shown in Table 2. At first, the TC11 wire was deposited on TC11 alloy substrate to a height of 60 mm. Subsequently, the TC4 wire was deposited on the as-deposited TC11 up to a total height of 120 mm. The schematics of the MWAAM Ti basic gradient heterogeneous alloy component and deposition scanning pattern are shown in Fig. 1.

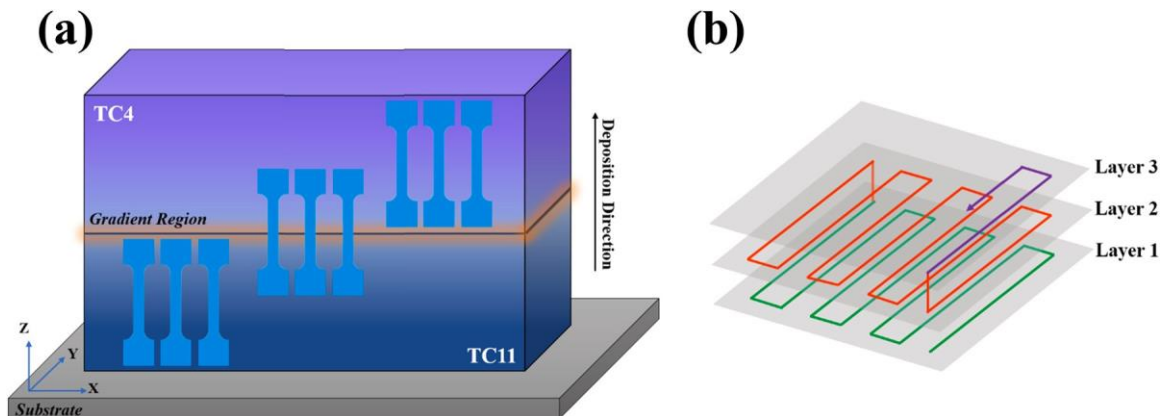


Fig. 1. (a) Schematics of the MWAAM Ti basic gradient heterogeneous alloy component, (b) deposition scanning pattern.

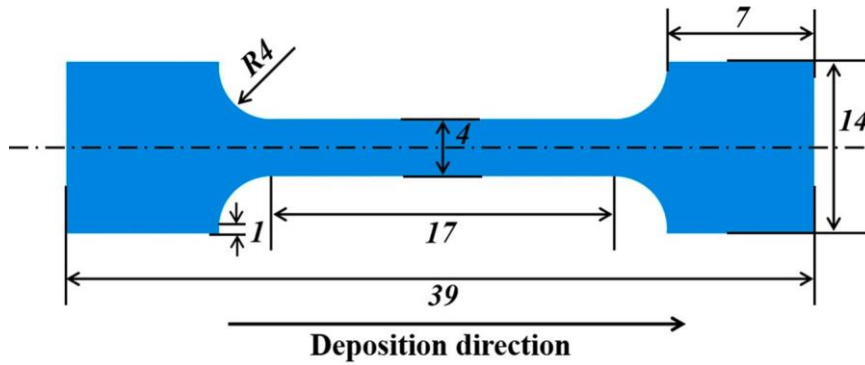


Fig. 2. Shape and dimensions (units: mm) of tensile specimens.

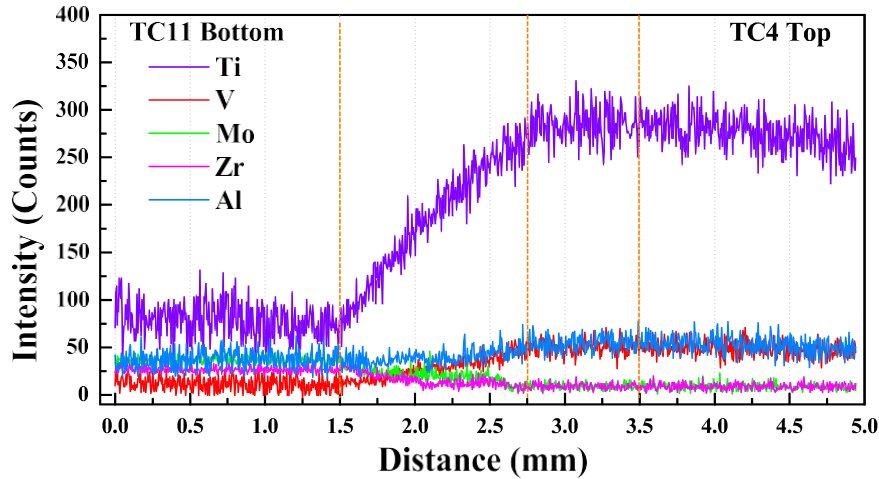


Fig. 3. The distribution of compositions in the interface of MWAAM Ti basic gradient heterogeneous alloy.

2.2. Material characterization

After MWAAM process, the as-built specimens were spark cut for microstructural characterization and mechanical test. The shape and dimensions of tensile specimens are displayed in Fig. 2. To investigate the chemical gradient and phase formed in the transition region, the energy-dispersive X-ray spectrometer (EDS, JSM-IT500A) and X-ray diffraction (XRD, D/Max 2500PC, Rigaku, Cu K α) were performed normal to the layers. The grain morphology and microstructure of cross-section of specimen parallel to deposition direction were observed via optical microscopy (OM, ZEISS-Scope A1) and scanning electron microscopy (SEM, JSM-IT500A) after standard metallographic procedure of grinding, polishing, and etching with a solution (1 ml HF, 6 ml HNO₃ and 100 ml H₂O) for 10 s

2.3. Microhardness and tensile testing

The microhardness of cross-section of specimen was performed using a Vickers automatic hardness tester (Huayin, HVS-1000), with a test load of 200 g and dwell time of 15 s. The position was tested every 0.5 mm from TC11 alloy side to TC4 alloy side, and each position for three times to take the average value to reduce the error. Tensile properties at room temperature were conducted on a tensile testing machine (Instron 1121). The constant displacement rate was 1 mm/min. The fracture morphologies of the failed specimens were analyzed by the same SEM as stated above and ultra-depth of field 3D microscope (VHX-950 F) to evaluate the tensile failure mechanisms.

3. Results and discussion

3.1. Transition overviews

In order to study the chemical gradient formed during the transformation from TC11 alloy to TC4 alloy, EDS line scanning analysis was carried out in the direction perpendicular to each layer. EDS maps for interface regions are presented in Fig. 3. The EDS results showed that the alloy elements formed a long-distance gradient concentration distribution during the deposition of TC4 on TC11. Driven by the complex convection of liquid in the moving process of molten pool, the solute between the new layer of wire deposition and the remelting volume of the previous layer was mixed in the molten pool, and then retained with the solidification process. There are relatively many related literatures reported the molten pool circulation driven by arc force convection, but the surface tension gradient of liquid metal is also one of the important reasons for the formation of convection [25]. The temperature of the molten pool liquid under the arc is the highest and the surface tension of the liquid is the lowest. The surface tension of the liquid increases when the temperature of the liquid decreases away from the arc center. The liquid far from the arc center will pull away from the arc center due to the increase of surface tension, which will reduce the height of the liquid surface under the arc and increase the height of the liquid surface far away from the deposition direction. A liquid gravity countercurrent will be generated below the high liquid level with the increase of this height difference, so that the liquid countercurrent will return to the lower liquid level area below the arc, as shown in Fig. 4. The convection cycle on the liquid surface will move

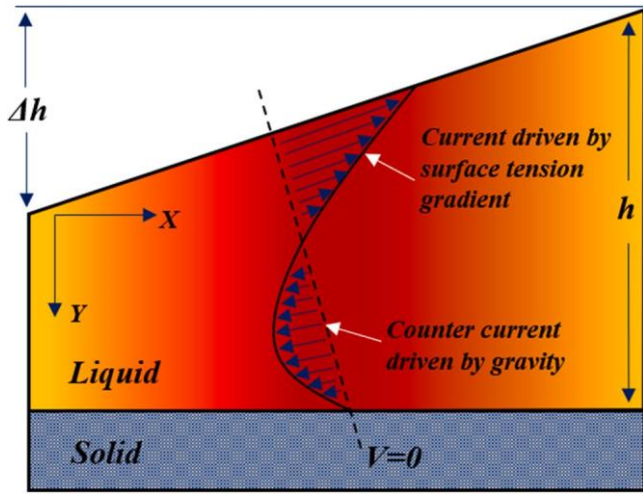


Fig. 4. The flow pattern of thin liquid layer with surface tension gradient on the surface.

Table 3
Average layer compositions measured from the EDS data for the MWAAM specimen base alloys and 3 layers after deposition of the new alloy.

Specimen	Layer	Mo (wt%)	Zr (wt%)	V (wt%)
TC11 bottom		3.34	1.69	0
	1	1.75	0.82	0.34
	2	0.78	0.36	0.84
TC4 top	3	0.24	0.16	2.02
		0	0	3.96

continuously when the arc moves, resulting in the dilution effect of the previous layer on the newly added layer. TIG arc heat source is used in WAAM, and standard process parameters are optimized to avoid fusion defects. This requires a remelting depth of about 0.7 mm, resulting in a dilution level of 50–70% between each layer [15,26]. For WAAM, if another alloy wire is added to the previously deposited substrate, and then the effect of dilution on element concentration (if this element does not exist in the new alloy wire) $C_{x,n}$, can be simply predicted using the following relationship [15]:

$$C_{x,n} = C_{x,o} [F_d]^n \quad (1)$$

Where $C_{x,o}$ is the initial concentration of elements in the base layer, F_d is the dilution of the added new alloy, and n is the number of deposition layers. Thus, it can be estimated that the average dilution of TC4 alloy deposited on TC11 alloy was 47% according to the results of Table 3.

In order to explore the microstructure evolution after the first layer of TC4 deposited on TC11 alloy, OM observation at lower magnification was carried out. The OM results indicated that the microstructure of the interface between the first TC4 alloy layer and the last TC11 alloy layer changed obviously, as shown in Fig. 5. After deposited the first layer of TC4 alloy, the microstructure below the bonding zone gradually coarsened from TC11 layer to TC4 layer. When the first TC4 layer was deposited on the last TC11 layer, the alloy elements in the newly deposited TC4 layer and the elements in the TC11 remelting zone will be completely mixed in the whole new melting zone due to the complex heat flow cycle in the molten pool. Therefore, part of the deposited layer as a new remelting zone will be diluted again during the deposition of the next TC4 layer, although the dilution degree was low. Meanwhile, violent component diffusion will occur due to high temperature in the lower part of the deposited layer near the molten pool. Two diffusion zones will be formed when depositing the first TC4 layer, and the content of Mo and V elements will change linearly in the diffusion zone, as shown in Fig. 6. With the repetition of this process, the elements in TC11 sedimentary layer can be transferred upward through many subsequent sedimentary layers added later. As shown in Fig. 7, the element diffusion decay rate depends on the dilution level [15]. It can be seen from Fig. 7 that, the remelting depth was large at a high dilution level, and the matrix elements can diffuse into more deposited layers. However, the remelting depth was small at a small dilution level and the element diffusion distance was short. In addition, the concentration of alloying elements in the base alloy will decay to a very low level when it exceeded the third deposition layer. Therefore, a certain width of gradient diffusion region will be formed during the preparation of WAAM dissimilar alloys, and the width of the gradient diffusion region can be determined in advance by intelligent control of WAAM deposition process parameters.

3.2. Phase composition

The phase composition analysis of the gradient region between TC11 alloy and TC4 alloy was examined by X-ray diffraction test. Three positions were tested (named T/T-1, T/T-2 and T/T-3) in the

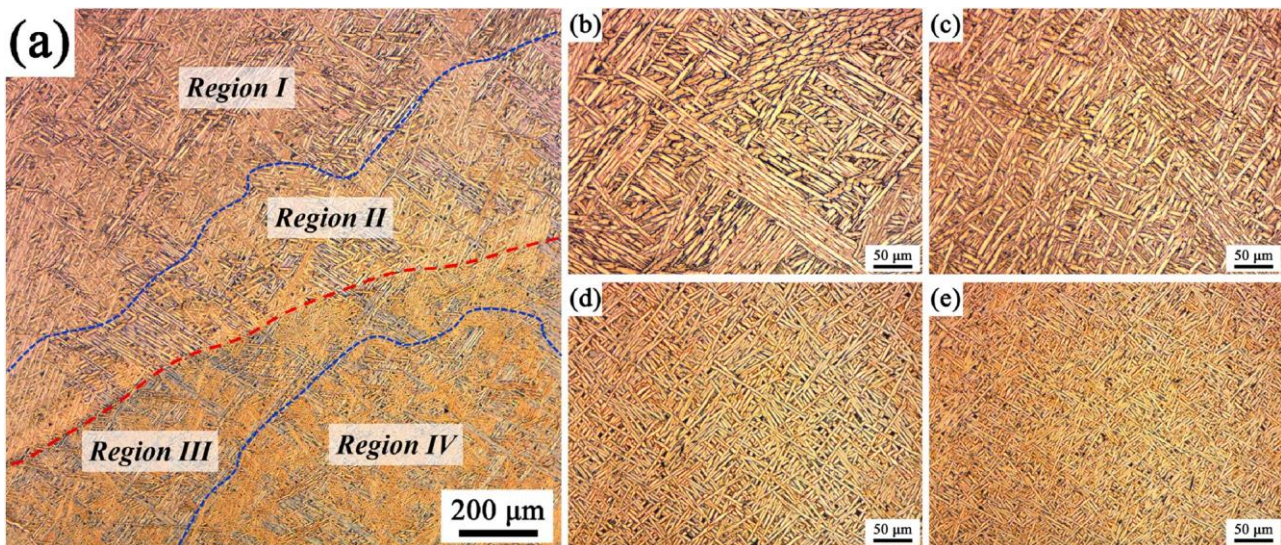


Fig. 5. OM microstructure (X-Z plane) of MWAAM Ti basic gradient heterogeneous alloy: (a) Gradient region; (b) Region I; (c) Region II; (d) Region III; (e) Region IV.

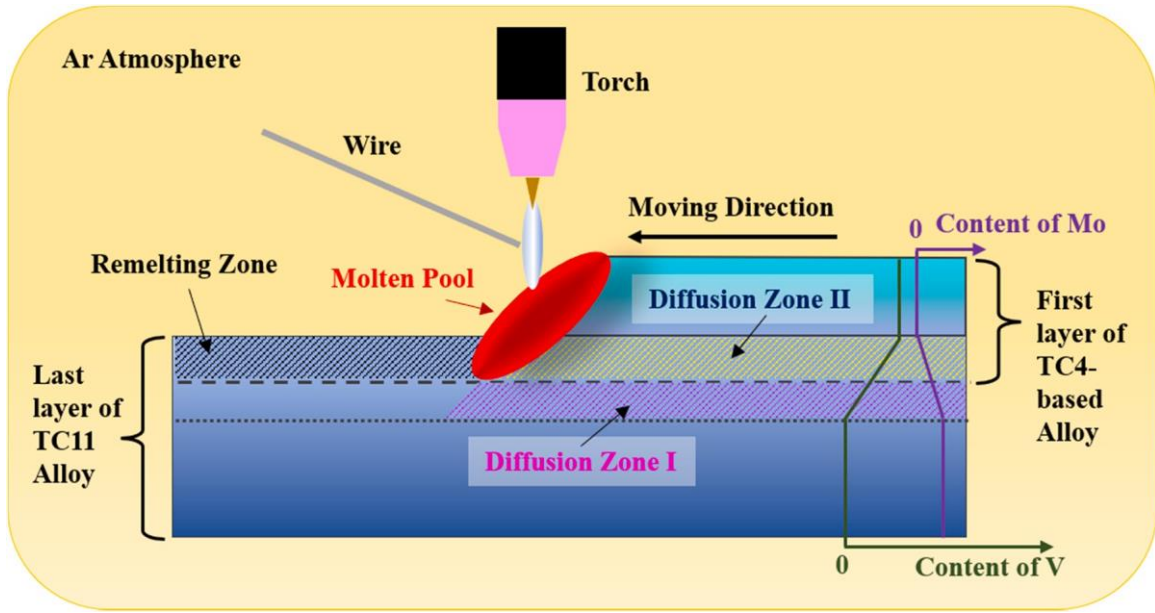


Fig. 6. Schematic view of interface when depositing the first layer of TC4 alloy.

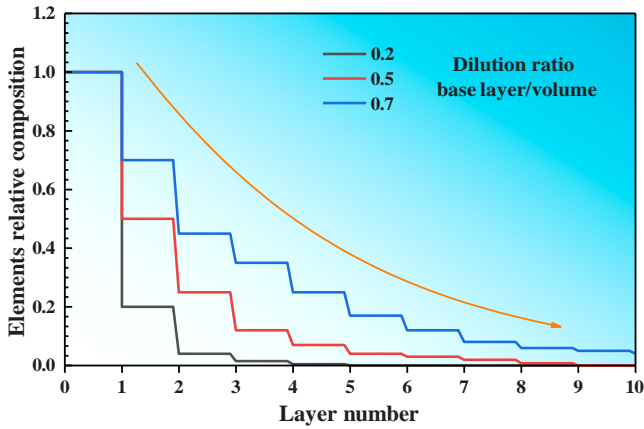


Fig. 7. The theoretical composition profile of an alloy element through multiple added layers of a dissimilar alloy wire with different dilution ratios (adapted from Kennedy et al., 2021).

gradient region parallel to the deposition direction from TC11 alloy to TC4 alloy. The X-ray diffraction patterns of the as-received Ti basic gradient heterogeneous specimens are shown in Fig. 8. All the specimens exhibited a typical hexagonal close-packed (HCP) α phase and body-centered cubic (BCC) β phase. It can be seen from Fig. 8a that the intensity of diffraction peaks in the gradient region had no obvious change. However, the intensity of α (100) peak and α (201) peak in TC4 alloy and α (103) peak in TC11 alloy were higher than that of the diffraction peak in the gradient region. Moreover, the α (101) diffraction peak of three gradient regions shifted to a higher angle compared with the α (101) peak of TC11 and TC4 alloys, as shown in Fig. 8b. This phenomenon can be attributed to that the radius of V atom (0.132 nm) was smaller than that of Mo atom (0.136 nm). The lattice parameter of α -Ti was reduced with the

increase of V element content. According to the Bragg equation, the decreased of lattice constant will increase the diffraction angle, and then the diffraction peak will shift to the higher angle [27,28]. The main α diffraction peak angles and full width at half maximum (FWHM) of each specimen were calculated by Jade 6 analysis software, and the results are shown in Table 4. It can be concluded that the FWHM of specimens from T/T-1 to T/T-3 in the gradient region was gradually decreased, and the FWHM of TC11 alloy specimen was larger than that of the TC4 alloy specimen from Table 4. This might be due to the high content of element solute in the gradient region, which resulted in the deformation of crystal structure and further changed in the FWHM of the diffraction peak [29,30].

3.3. Microstructure

For TC11 and TC4 titanium alloys, when the temperature is first cooled below the β -phase transition point during the MWAAM process, the α -phase mainly appears in two forms [31–33]: (1) α phase nucleates on β grain boundaries to form allotropes and single variant α colonies (Widmandelstein); (2) α phase nucleates in β grain to form high aspect ratio laths in multi variant laths with interlocking basket morphology. Since no new phase is expected to form in the intermediate composition of the TC11-TC4 heterogeneous alloy system, it is expected that the microstructure will gradually change between TC11 and TC4 during the gradient diffusion process of the alloy. In order to investigate the microstructure changes of Ti basic gradient heterogeneous alloy, the junction of the last layer of TC11 and the first layer of TC4 was taken as the central origin ($x = 0$), and six positions were observed parallel to the deposition direction (from TC11 to TC4: $x = -3$ mm; $x = -2$ mm; $x = -1$ mm; $x = 0$ mm; $x = 1$ mm and $x = 2$ mm). Fig. 9 shows the different positions microstructure of Ti basic gradient heterogeneous alloy specimens. It can be seen from Fig. 9 that the microstructure showed a gradually change and the size of α precipitates showed a gradually increased

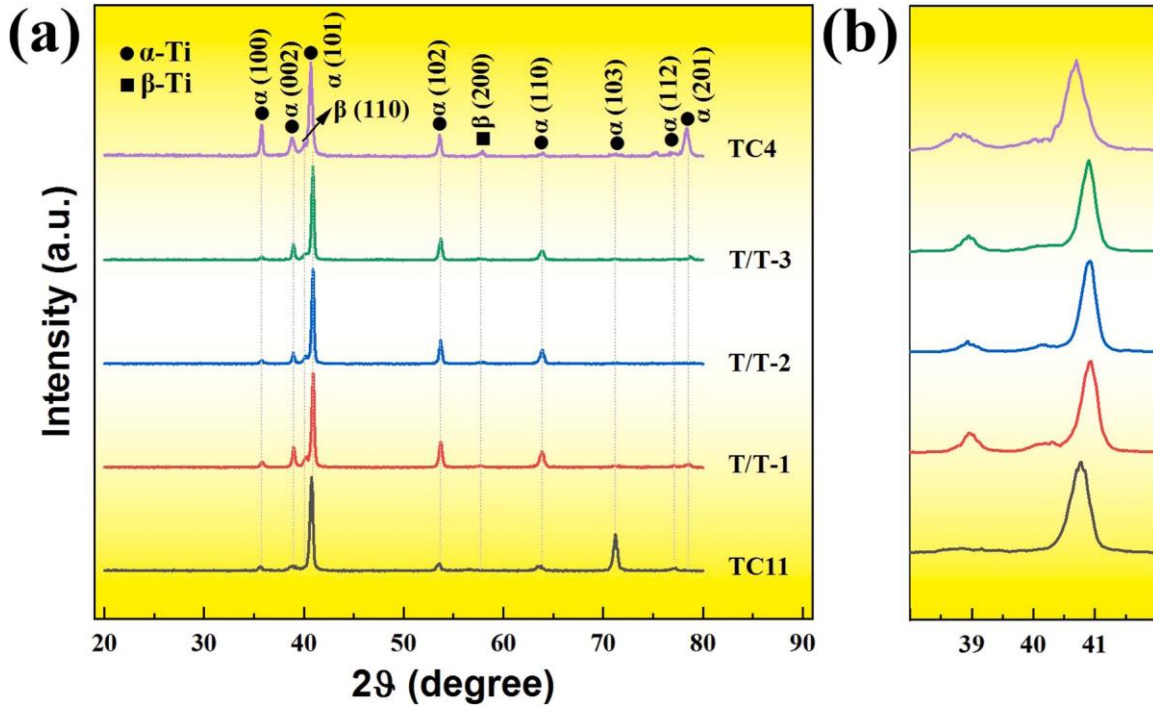


Fig. 8. (a) XRD patterns of MWAAM Ti basic gradient heterogeneous specimens at different positions, (b) partial enlarged pattern of XRD.

Table 4
XRD data for MWAAM Ti basic gradient heterogeneous alloy.

Specimen	Miller indices	α (100)	α (002)	α (101)
TC4	2 θ	35.799	38.861	40.699
	FWHM	0.274	0.347	0.306
T/T-3	2 θ	35.701	38.959	40.900
	FWHM	0.333	0.239	0.296
T/T-2	2 θ	35.700	38.938	40.919
	FWHM	0.394	0.261	0.304
T/T-1	2 θ	35.843	38.961	40.920
	FWHM	0.379	0.279	0.342
TC11	2 θ	35.584	38.781	40.760
	FWHM	0.279	0.422	0.368

during the transition from TC11 alloy to TC4 alloy. This progressive microstructural change was mainly due to the insensitivity of α nucleation to the dilution of β stabilizing elements [24]. Kennedy et al. [15] reported the microstructural evolution of the Ti-5553→Ti-64 alloy transition region. They found that the β -transition temperature and the diffusion transformation kinetics will increase with the decrease of molybdenum content during the transition from Ti-5553 alloy to Ti-64 alloy due to the low transformation temperature and diffusivity of molybdenum. Therefore, the microstructure gradually coarsens in morphology as the β -transition temperature and the diffusion rate of the partitioning elements increase. This result is consistent with the phenomenon observed in this experiment. Moreover, Imagine J software was used to calculate the proportion of the two phases of Fig. 9a-f, and the results are shown in Table 5. The results show that the proportion of α phase increases gradually

during the microstructure transition from TC11 to TC4. The α phase proportion increased from 56.60% to 69.67%, while the β phase proportion decreased from 43.40% to 30.33%.

Fig. 10 shows the microstructure at the bonding interface in the gradient region of Ti basic heterogeneous alloys. It can be seen from the Fig. 10a-b that there had obvious continuous transformation in the microstructure at the bonding interface. The α strip structure of near TC11 alloy side was thinner than the side near TC4 alloy. Fig. 10c is a partially enlarged view of Fig. 10b. It can be seen that the microstructure of near TC4 side was mainly composed of lamellar primary α phase (α_P) and intergranular β , and the microstructure of near TC11 side was mainly composed of lamellar primary α phase (α_P) and transformed β phase (β_T). This was due to that the molybdenum content in TC4 alloy was lower than that in TC11 alloy and molybdenum was stable element of β phase, thus the size α phase in MWAAM TC4 alloy was larger than MWAAM TC11 alloy. In addition, the β phase transition temperature of TC11 alloy was higher than TC4 alloy, resulting in the fraction of the β phase in TC11 alloy was higher than TC4 alloy. This result is consistent with the change trend of phase distribution proportion in Fig. 9 above. However, it can be found that secondary α phase in the β matrix was different on the two sides of bonding interface, as shown in the Fig. 11. It can be seen that from Fig. 11a-b, no secondary α phase was found in microstructure of intergranular β region near the TC4 alloy side. The microstructure of β_T region near the TC11 alloy side was composed of secondary α phase (α_S) (including acicular secondary α phase and equiaxed secondary α phase) and β matrix, as shown in Fig. 11c-d. Different from the previously reported work [24], the equiaxed α_S phase was found in the preparation of MWAAM Ti basic gradient heterogeneous alloys.

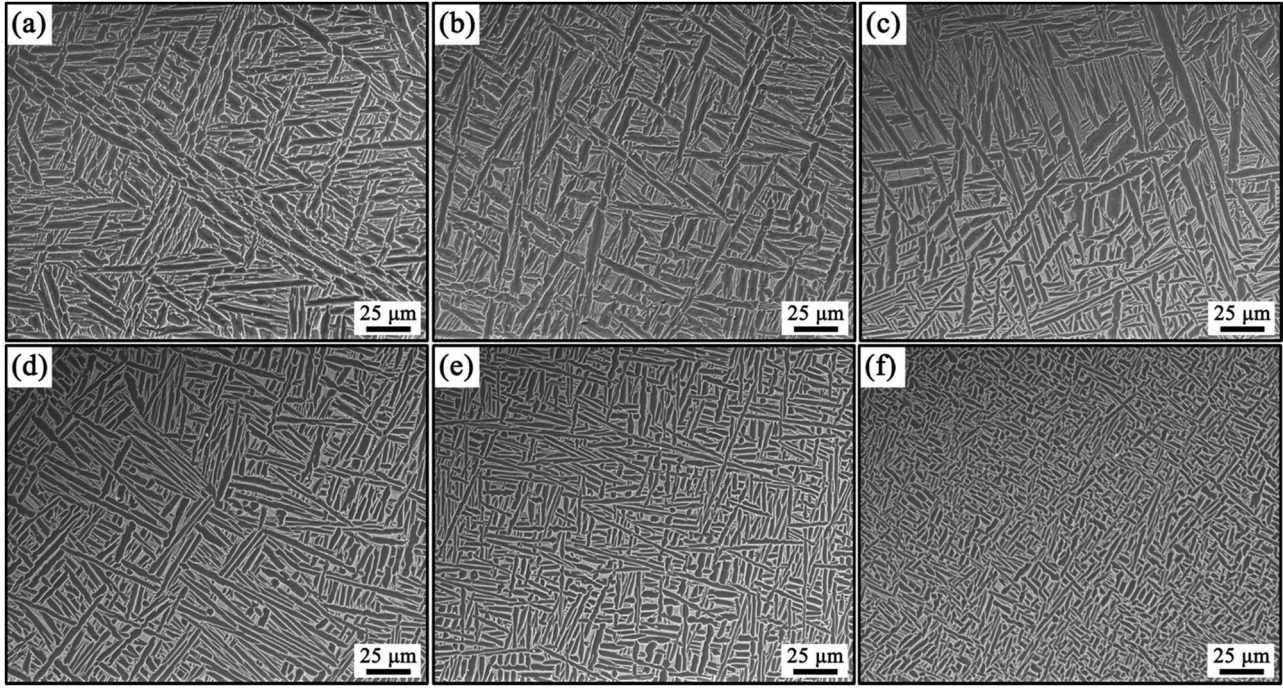


Fig. 9. The SEM microstructure (X-Z plane) of different positions around the interface: (a) $x = 2$ mm; (b) $x = 1$ mm; (c) $x = 0$ mm; (d) $x = -1$ mm; (e) $x = -2$ mm; (f) $x = -3$ mm.

Table 5

The phase proportion of the MWAAM Ti basic gradient heterogeneous alloy.

	$X = 2$	$X = 1$	$X = 0$	$X = -1$	$X = -2$	$X = -3$
α (%)	69.67	67.57	60.71	59.67	58.98	56.60
β (%)	30.33	32.43	39.29	40.33	41.02	43.40

The precipitation of α_s phases is closely related to the complete and incomplete wetting of grain boundary by the second solid phases [34]. The schematic diagram of polycrystals with different wetting angles of the second phase is shown in Fig. 12. When the second solid phase was completely wetted, the contact angle $\theta = 0^\circ$, as shown in Fig. 12a. The contact angle θ would change when the second solid phase was not fully wetted (such as $\theta = 30^\circ, 90^\circ$) as shown in Fig. 12b-c. In addition, Gornakova et al. [34] found that changed in temperature and elements concentration can alter the contact angle of second phase. In the present study, the incomplete wetting of β/β grain boundaries plays a key role in the formation of equiaxed α_s under the condition of non-equilibrium solidification. As we all know, α_s phase preferred at β/β grain boundary precipitation when cooling of the $\alpha + \beta$ two-phase zone. Actually, the phenomenon of α_s precipitated around β/β grain boundary belongs to a typical heterogeneous nucleation. The thermodynamic formula for the nucleation of α_s on grain boundaries can be expressed as follows [35]:

$$\Delta G_s = V^\alpha \Delta G_V + A_{\alpha\beta} \gamma_{\alpha\beta} - A_{\beta\beta} \gamma_{\beta\beta} \quad (2)$$

where V^α is the volume of α_s nucleus, ΔG_V represents the free energy released per unit volume of β to α transition, and γ is interface energy per unit area. The α_s phase nucleation barrier ΔG_s^* according to the classical nucleation theory can be described as follows [36]:

$$\Delta G_s^* = \Delta G_h f(\theta) \quad (3)$$

$$f(\theta) = (2 - 3\cos\theta + \cos^3\theta) / 2 \quad (4)$$

where ΔG_h represents energy barrier of homogeneous nucleation. It can be seen from Eqs. (3) and (4) that the nucleation barrier in heterogeneous nucleation is less than that in homogeneous nucleation for α_s phase formation. In this case, the following equation is given as [35]:

$$2\cos\theta = \gamma_{\beta\beta} / \gamma_{\alpha\beta} \quad (5)$$

Based on the Eq. (5), the morphology of secondary α phase was determined by the ratio of $\gamma_{\beta\beta}$ and $\gamma_{\alpha\beta}$. When the interfacial energy α/β was low and the $2\gamma_{\alpha\beta}$ was less than $\gamma_{\beta\beta}$, the contact angle θ would be 0° . The morphology of secondary α phase was mainly consisted of lamellar and acicular. However, the temperature fluctuation of the molten pool increased due to the TC11 and TC4 alloys had a long element concentration gradient in the bonding region, resulting in the incoherent α/β interfaces formed and the value of $\gamma_{\alpha\beta}$ increased [35,37]. When the $2\gamma_{\alpha\beta}$ was higher than $\gamma_{\beta\beta}$, the contact angle θ will form a certain angle and the equiaxed secondary α phase will also appear. In addition, the heterogeneous nucleation at the dislocation will also promote the morphology of α_s changes from lamellar to equiaxed due to the decrease of the nucleation barrier and the high nucleation density [38].

3.4. Mechanical properties

The microhardness distribution of the gradient area from bottom region (TC11 alloy) to the top region (TC4 alloy) in the cross-sectional plane of the MWAAM Ti basic gradient heterogeneous alloy specimen is presented in Fig. 13. Similar to the element distribution curve, the microhardness curve showed a gradient fluctuation characteristic. The microhardness values on both sides of the specimen fluctuated within a certain range, and the change was not obvious. With the deposition of TC4 alloy on TC11 alloy, the interlayer hardness value decreased greatly and the fluctuation range increased. This phenomenon can be explained by the following two

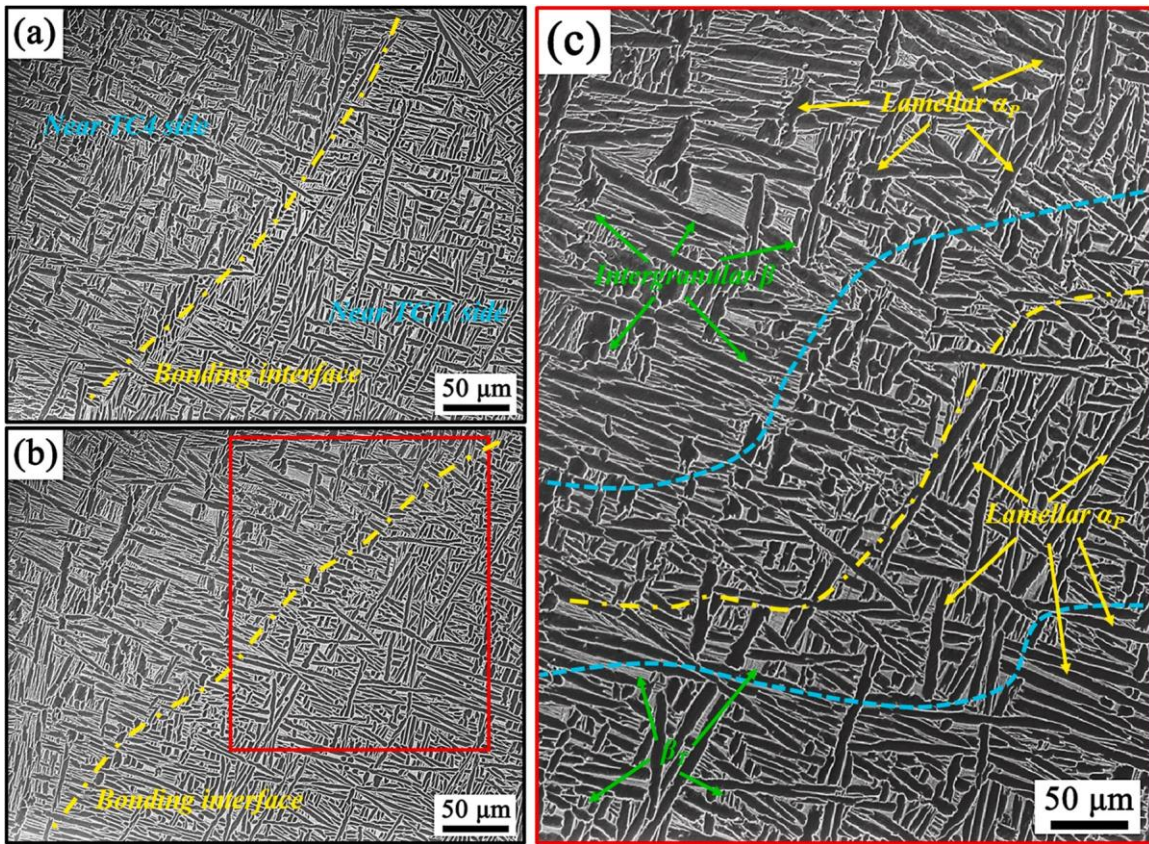


Fig. 10. The SEM microstructure (X-Z plane) at the bonding interface in the gradient region of MWAAM Ti basic heterogeneous alloy.

reasons: (1) Solute elements decreased resulting in lattice distortion decreased with the deposition of TC4 alloy. Under the action of external force, lattice deformation became easier. (2) The coarsening of microstructure reduced the proportion of phase boundary and promoted local crystal sliding.

Fig. 14 shows the tensile stress-strain curves of MWAAM TC11, TC4, and Ti basic gradient heterogeneous alloy specimens (T-T-1, T-T-2, and T-T-3) at room temperature. The results of tensile test are listed in Table 6. The yield strength (YS) of T-T-1, T-T-2, and T-T-3 specimens were between TC11 and TC4 alloy specimens, indicating that TC4 alloy specimen began to yield earlier and plastic deformation was easier than other specimens. The average YS of Ti basic gradient heterogeneous alloy specimens was 770.89 MPa. The average total elongation (EL) of Ti basic gradient heterogeneous alloy was 5.42%, which was smaller than that of TC4 and TC11 alloy specimens. From the stress-strain curve, it can be seen that the ultimate tensile strength (UTS) of Ti basic gradient heterogeneous alloy specimens was 774.78 MPa ~ 819.08 MPa, and the average tensile strength was similar to that of TC4 alloy. The maximum tensile strength of Ti basic gradient heterogeneous alloy reached 88% of that of the Ti-6Al-4 V/Ti-6.5Al-3.5Mo-1.5Zr-0.3Si graded structural material deposited by laser melting deposition [23]. Three Ti basic gradient heterogeneous alloy specimens all fractured on the side of

TC4 alloy. Overall, Ti basic gradient heterogeneous alloy specimens had good tensile properties at room temperature due to that the good metallurgical bonding with high strength was obtained in the gradient region. It was notable that the UTS of some gradient heterogeneous specimens was higher than that of TC4 alloy specimen in this work. This may be related to the formation of a longer chemical concentration gradient in the bonding region of the two heterogeneous alloy materials. This special structure can maintain the coordination and uniform deformation between TC11 and TC4 alloy, promote the uniform deformation within the gauge distance, and delay the development of necking [39]. In addition, the secondary α phase generated in the gradient region will form lattice distortion and increase the interface energy. These factors lead to the increase of the resistance of dislocations passing through the grain boundary, and the dislocations moving to the grain boundary will be pinned at the grain boundary, forming high-density dislocations. With the progress of loading, the density of dislocations will continue to increase, and the mutual delivery of dislocation movement will intensify, resulting in dislocation pile-up group, entanglements and other obstacles to hinder the further movement of dislocations, thus strengthening the pinning effect of dislocations [23]. Therefore, the UTS of Ti basic gradient heterogeneous alloy specimens was improved. Moreover, the T-T-1, T-T-2, and T-T-3 specimens showed

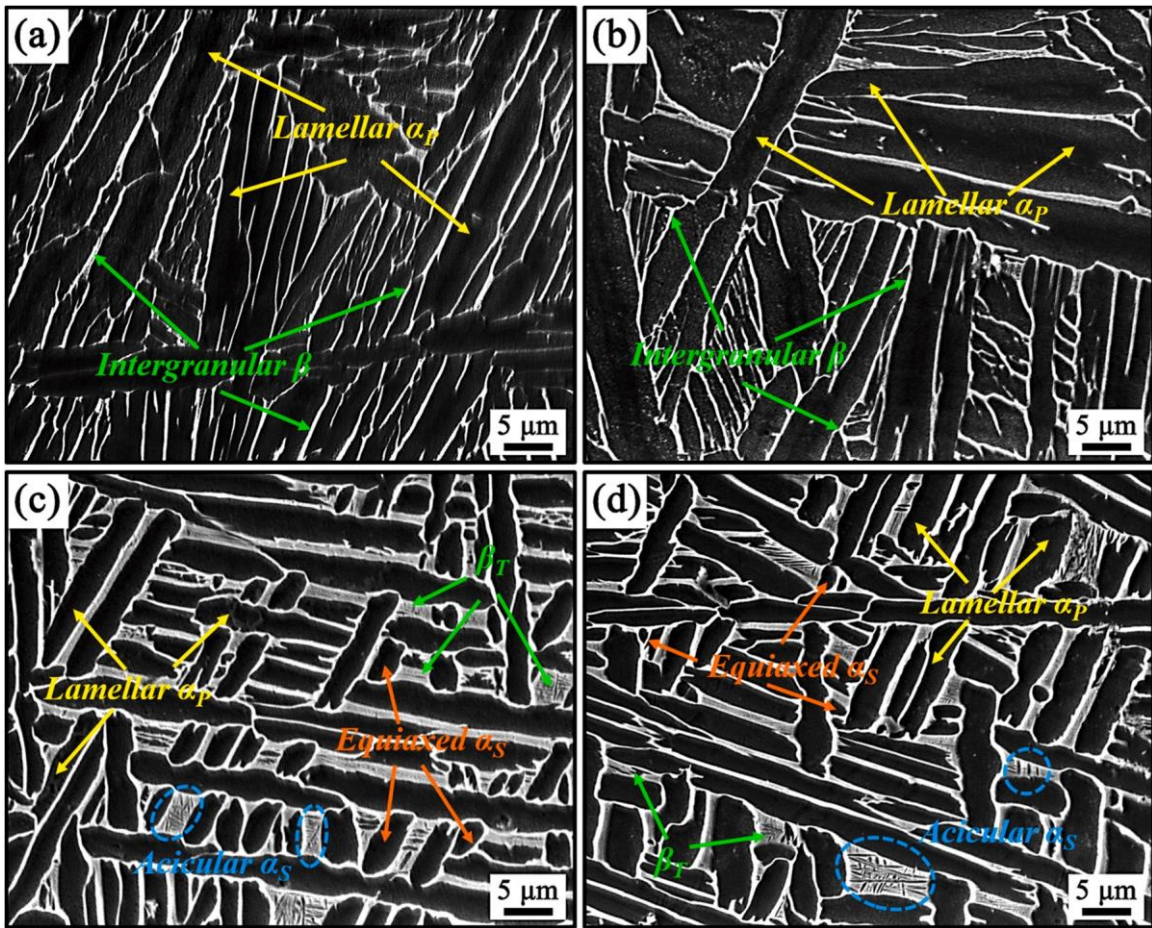


Fig. 11. High magnification SEM (X-Z plane) of microstructure at the bonding interface in the gradient region of Ti basic heterogeneous alloys: (a) and (b) near the TC4 alloy side; (c) and (d) near the TC11 alloy side.

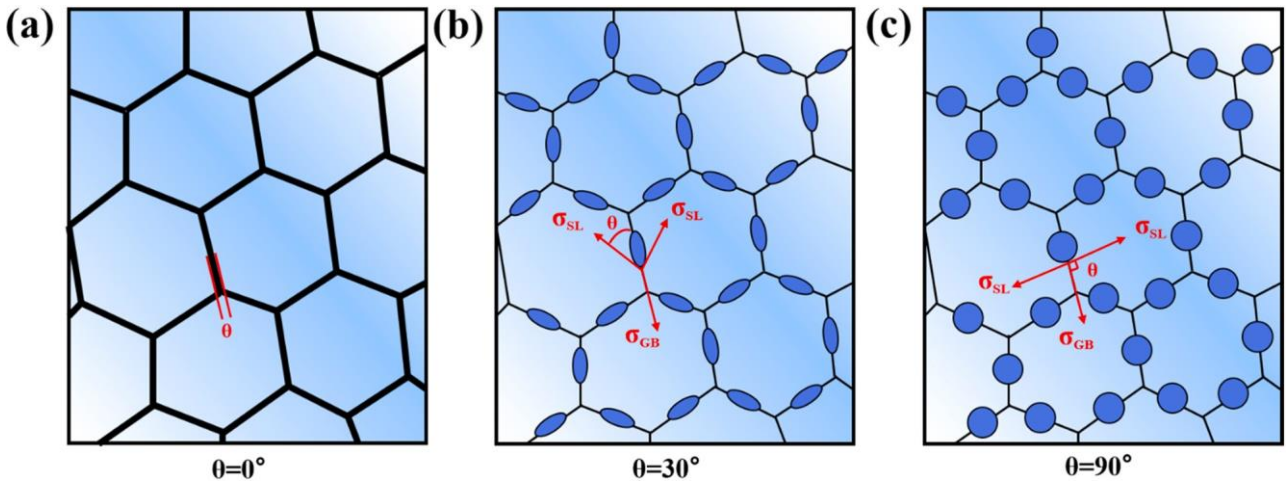


Fig. 12. Schematic diagram for second solid phase nucleation at grain boundary with three different wetting angles. The σ_{GB} and σ_{SL} are free energies of the unit area of surface GBs and liquid-solid interface, respectively.

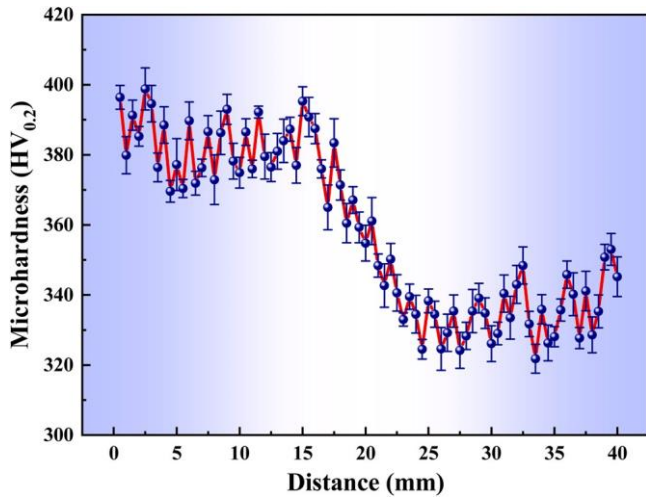


Fig. 13. The microhardness value of MWAAM Ti basic gradient heterogeneous alloy along the compositional gradient.

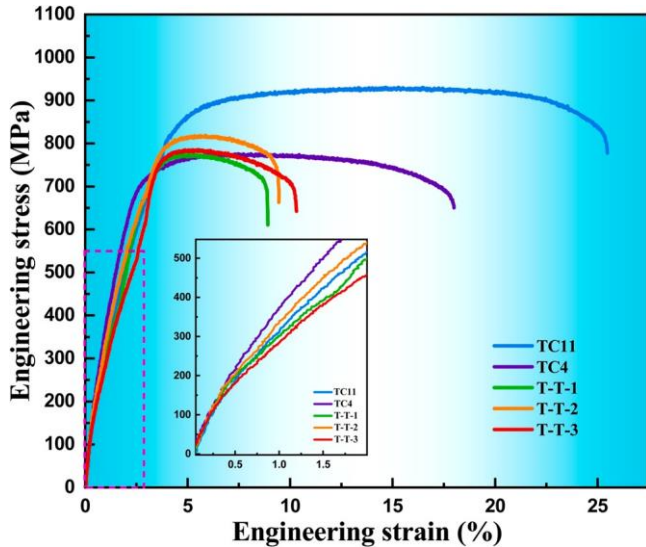


Fig. 14. The engineering stress-strain curve of different MWAAM specimens.

Table 6
Tensile properties (room temperature) of WMAAM specimens.

Specimen	UTS (MPa)	YS (MPa)	EL (%)
TC11	934.00 ± 6.09	854.59 ± 11.49	11.83 ± 1.27
TC4	783.90 ± 6.02	727.96 ± 18.89	8.14 ± 1.58
T-T-1	774.78	755.54	5.28
T-T-2	819.08	789.66	5.44
T-T-3	785.57	767.46	5.54

strain hardening after the beginning of plastic deformation from Fig. 14. Then, the strain hardening rate decreased. The specimens would begin to strain soften until it broke when a certain strain was reached. The strain hardening rates of the other two types of specimens (TC4 and TC11 alloys) were almost the same and constant in the plastic deformation zone. The fracture strain of TC11 and TC4

alloy specimens was higher than that of Ti basic gradient heterogeneous alloy specimens. Therefore, Ti based gradient heterogeneous specimens may need post-treatment, such as heat treatment or interlaminar rolling, to achieve improved ductility.

Tensile fracture can further understand the influence of microstructure on mechanical properties. The fracture morphologies of MWAAM TC11, TC4 and T-T-1 specimens after the room temperature tensile test as shown in Fig. 15. The ductile fracture surface with elongated necking was observed in the macro morphology of the fracture surface of the three specimens, as shown in Fig. 15a-c. The higher-magnification SEM images of the MWAAM TC11, TC4 and T-T-1 specimens are shown in Fig. 15d-f. It can be seen from the Fig. 15d that the surface fracture morphology of TC11 alloy specimen included typical river patterns and smooth dimples. However, the dimples of TC4 and T-T-1 specimens were relatively shallow and large compared with TC11 specimen. The small and deep dimple shape indicated that the toughness was better during tensile deformation [40,41]. As we all know, the plastic deformation resistance of the α and β phases is different in dual-phase titanium alloys. The α phase was HCP structure and β phase was BCC structure. Generally, BCC structures had stronger plastic deformation resistance than HCP structures. As can be seen from Table 5, the proportion of β phase was the highest on TC11 alloy side and the lowest on TC4 alloy side. Therefore, TC11 alloy specimen can withstand greater plastic deformation. This phenomenon was consistent with the highest elongation of TC11 specimen in all tested specimens. Meanwhile, the surface fracture morphology of T-T-1 alloy specimen was similar to the TC4 alloy specimens due to the fracture position of T-T-1 specimen was at TC4 side. Zhang et al. [42] had investigated the effect of microstructure on the tensile property of TC21G titanium alloy. They found that the increase of the size and content of acicular α phase in β matrix will lead to the increase of the degree of crack deflection during the tensile process, resulting in more tortuous and longer growth path of cracks, thus improving the alloy plasticity. Therefore, adjusting the microstructure of the Ti basic gradient heterogeneous alloy prepared in this paper by heat treatment is expected to further improve the plasticity of the gradient heterogeneous alloy specimens.

Fig. 16 illustrates the representative fracture surfaces in the crack growth zone of tensile fracture of the as-built MWAAM Ti basic gradient heterogeneous alloy (but not in all specimens). As shown in Fig. 16a-b, two kinds of parabolic crack propagation paths were observed, one was that there were microcracks around the defect, and the other was that there were no microcracks around the defect. The cracks can produce two kinds of parabolic propagation when the main crack encountered defects in the tensile process. The reason for the formation of two kinds of parabolic propagation can be explained as following: when there were microcracks around the defect, the main crack would preferentially merge with the microcrack to form the first type of parabolic, as shown in Fig. 16a and c. However, when there were no microcracks around the defect and the main crack cannot pass through the defect during the propagation process, the propagation direction of the main crack would deflect around the defect to form the second type of parabolic, as shown in Fig. 16b and d. Therefore, reducing the crack growth rate by controlling was beneficial to improve the mechanical properties of the alloy. Similar conclusions had also been reported by Cui et al. [43]. In addition, they concluded that the difference of crack location had a greater influence on the mechanical properties of the alloy than the crack type.

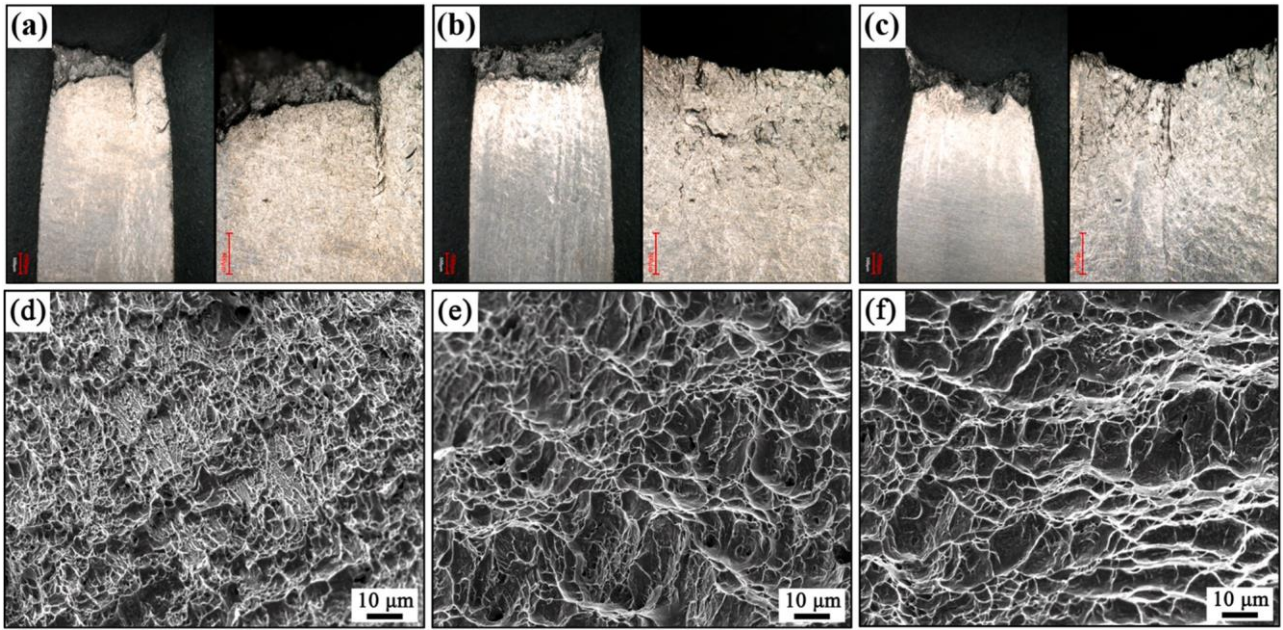


Fig. 15. (a)-(c) The low-magnification images of the fracture surfaces of MWAAM TC11, TC4 and T-T-1 respectively; (d)- (h) The high-magnification SEM micrographs of the tensile fracture surfaces of MWAAM TC11, TC4 and T-T-1 respectively.

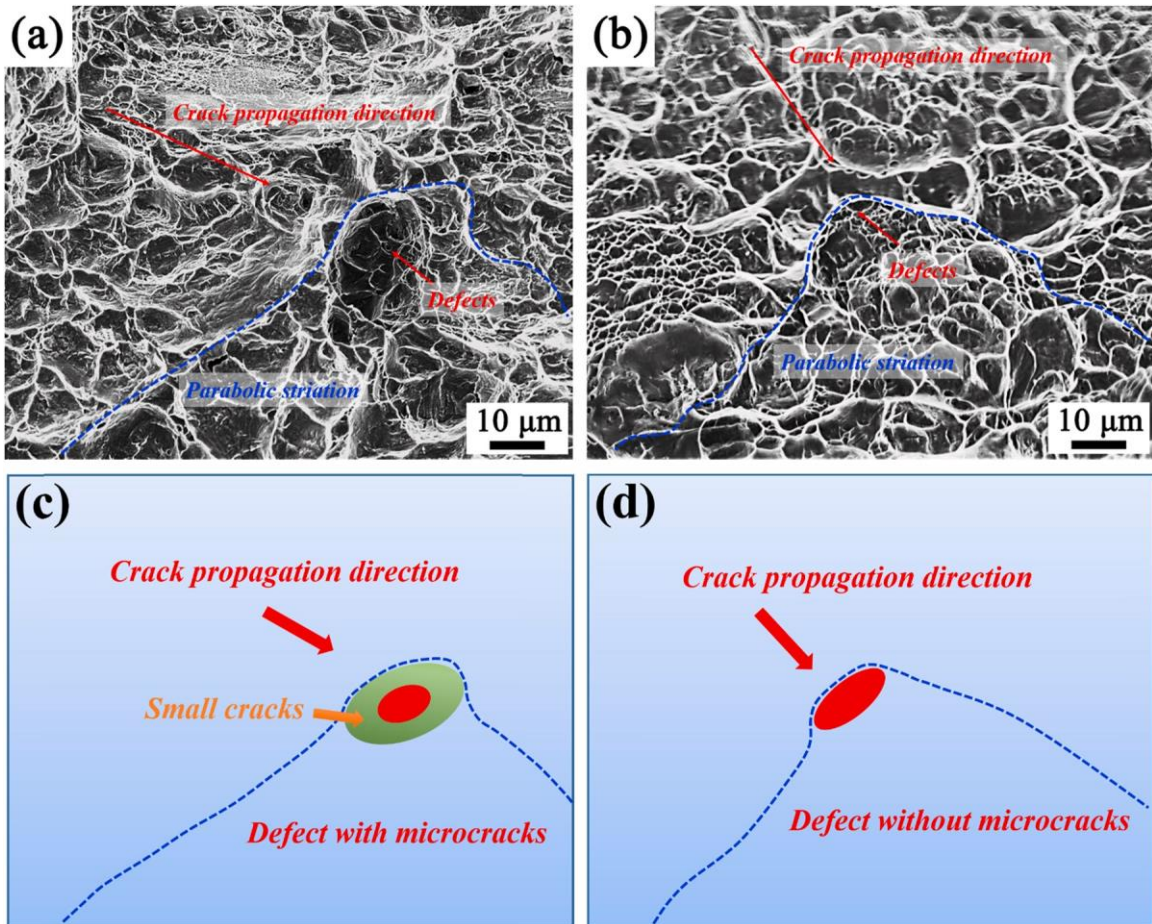


Fig. 16. Crack propagation regions of failed specimens: (a) and (c) MWAAM T-T-1 specimen; (b) and (d) MWAAM T-T-3 specimen.

4. Conclusions

- (1) The alloy elements formed a long-distance gradient concentration distribution during the transition between two different titanium alloys due to dilution, remelting, and convective mixing in the molten pool between the TC11 alloy and TC4 alloy. The surface tension gradient of liquid metal promoted the dilution of alloy elements in MWAAM process. The α (101) diffraction peak of three gradient regions shifted to a higher angle compared with the α (101) peak of TC11 and TC4 alloys due to that the lattice parameter of α -Ti was reduced with the increase of V element content.
- (2) The size and proportion of α precipitates showed a gradually increased during the transition from TC11 alloy to TC4 alloy. The microstructure of MWAAM Ti basic gradient heterogeneous alloy was mainly consisted of lamellar α_p , acicular α_s , equiaxed α_s and β matrix. Different morphology of the secondary α phase was mainly attributed to the wetting state of the second solid phase and grain boundary.
- (3) With the deposition of TC4 alloy on TC11 alloy, the interlayer microhardness decreased gradually. The average UTS and YS of MWAAM Ti basic gradient heterogeneous alloy were 793.14 MPa and 770.89 MPa respectively. The average UTS of MWAAM Ti basic gradient heterogeneous alloy was close to MWAAM TC4 alloy, and reached approximately 85% of MWAAM TC11 alloy. Such enhancement in the tensile strength can be ascribed to the formation of a longer chemical concentration gradient in the bonding region of the two heterogeneous alloy materials.
- (4) The surface fracture morphology of MWAAM Ti basic gradient heterogeneous alloy was similar to the MWAAM TC4 alloy specimens due to the fracture position was at TC4 side. MWAAM Ti basic gradient heterogeneous alloy was mainly ductile fracture. The tensile crack propagation zone was characterized by brittle fracture, occasional parabolic striations.

CRedit authorship contribution statement

P. F. Jiang: Writing – original draft. **X. R. Li:** Data curation. **X. M. Zong:** Formal analysis. **X. B. Wang:** Investigation. **Z. K. Chen:** Data curation. **C. Z. Liu:** Formal analysis. **N. K. Gao:** Investigation. **Z. H. Zhang:** Validation.

Data availability

No data was used for the research described in the article.

Declaration of Competing Interest

The authors declare that they have no known competing financial interests or personal relationships that could have appeared to influence the work reported in this paper.

Acknowledgments

This work is supported by National Natural Science Foundation of China (Grant 52025053), the Key Project of Science and Technology of Jilin Province (Grant No. 20220204119YY) and the Research Funds from Jiangsu Xuzhou Construction Machinery Research Institute Co., Ltd. (No. HT069–2021).

Data availability

The raw/processed data required to reproduce these findings cannot be shared at this time as the data also forms part of an ongoing study.

References

- [1] J. Wang, Z.X. Pan, K. Carpenter, J. Han, Z.Y. Wang, H.J. Li, Comparative study on crystallographic orientation, precipitation, phase transformation and mechanical response of Ni-rich NiTi alloy fabricated by WAAM at elevated substrate heating temperatures, *Mater. Sci. Eng. A* 800 (2021) 140307.
- [2] Tiago A. Rodrigues, V.R. Duarte, D. Tomás, Julian A. Avila, J.D. Escobar, Emma Rossinyol, N. Schell, Telmo G. Santos, J.P. Oliveira, In-situ strengthening of a high strength low alloy steel during Wire and Arc Additive Manufacturing (WAAM), *Addit. Manuf.* 34 (2020) 101200.
- [3] L. Palmeira Belotti, J.A.W. van Dommelen, M.G.D. Geers, C. Goulas, W. Ya, J.P.M. Hoefnagels, Microstructural characterisation of thick-walled wire arc additively manufactured stainless steel, *J. Mater. Process. Technol.* 299 (2022) 117373.
- [4] C.C. Su, X.Z. Chen, C. Gao, Y.F. Wang, Effect of heat input on microstructure and mechanical properties of Al-Mg alloys fabricated by WAAM, *Appl. Surf. Sci.* 486 (2019) 431–440.
- [5] O. Panchenko, D. Kurushkin, I. Mushnikov, A. Khismatullin, A. Popovich, A high-performance WAAM process for Al-Mg-Mn using controlled short-circuiting metal transfer at increased wire feed rate and increased travel speed, *Mater. Des.* 195 (2020) 109040.
- [6] Y.J. Li, Y.T. Yuan, D.X. Wang, S.C. Fu, D.R. Song, M. Vedani, X. Chen, Low cycle fatigue behavior of wire arc additive manufactured and solution annealed 308 L stainless steel, *Addit. Manuf.* 52 (2022) 102688.
- [7] Y.H. Chen, C.L. Yang, C.L. Fan, Y.M. Zhuo, S.B. Lin, C. Chen, Microstructure evolution mechanism and mechanical properties of TC11-TC17 dual alloy after annealing treatment, *J. Alloy. Compd.* 842 (2020) 155874.
- [8] S.H. Chen, Z.L. Zhai, J.H. Huang, X.K. Zhao, J.G. Xiong, Interface microstructure and fracture behavior of single/dual-beam laser welded steel-Al dissimilar joint produced with copper interlayer, *Int. J. Adv. Manuf. Technol.* 82 (2016) 631–643.
- [9] B. Onuik, A. Bandyopadhyay, Additive manufacturing of Inconel 718 – Ti6Al4V bimetallic structures, *Addit. Manuf.* 22 (2018) 844–851.
- [10] B. Onuik, A. Bandyopadhyay, Bond strength measurement for additively manufactured Inconel 718-GRCo84 copper alloy bimetallic joints, *Addit. Manuf.* 27 (2019) 576–585.
- [11] B.Y. Li, C.J. Han, C.W. Joel Lim, K. Zhou, Interface formation and deformation behaviors of an additively manufactured nickel-aluminum-bronze/15-5 PH multimaterial via laser-powder directed energy deposition, *Mater. Sci. Eng. A* 829 (2022) 142101.
- [12] S. Sridar, M.A. Klecka, W. Xiong, Interfacial characteristics of P91 steel-Inconel 740H bimetallic structure fabricated using wire-arc additive manufacturing, *J. Mater. Process. Technol.* 300 (2022) 117396.
- [13] Z.Q. Liu, M.A. Meyers, Z.F. Zhang, R.O. Ritchie, Functional gradients and heterogeneities in biological materials: Design principles, functions, and bioinspired applications, *Prog. Mater. Sci.* 88 (2017) 467–498.
- [14] M.K. Habibi, A.T. Samaei, B. Gheshlaghi, J. Lu, Y. Lu, Asymmetric flexural behavior from bamboo's functionally graded hierarchical structure: Underlying mechanisms, *Acta Biomater.* 16 (2015) 178–186.
- [15] J.R. Kennedy, A.E. Davis, A.E. Caballero, M. White, J. Fellowes, E.J. Pickering, P.B. Prangnell, Microstructure transition gradients in titanium dissimilar alloy (Ti-5Al-5V-5Mo-3Cr/Ti-6Al-4V) tailored wire-arc additively manufactured components, *Mater. Char.* 182 (2021) 111577.
- [16] J.Q. Li, X. Lin, Y. Yang, J. Wang, J.R. Liu, P.F. Guo, W.D. Huang, Distinction in electrochemical behaviour of Ti6Al4V alloy produced by direct energy deposition and forging, *J. Alloy. Compd.* 860 (2021) 157912.
- [17] J.J. Jiang, Z.H. Ren, Z.B. Ma, T. Zhang, P. Zhang, D.Z. Zhang, Z.F. Mao, Mechanical properties and microstructural evolution of TA15 Ti alloy processed by selective laser melting before and after annealing, *Mater. Sci. Eng. A* 772 (2020) 138742.
- [18] H.M. Hamza, K.M. Deen, W. Haider, Microstructural examination and corrosion behavior of selective laser melted and conventionally manufactured Ti6Al4V for dental applications, *Mater. Sci. Eng. C* 113 (2020) 110980.
- [19] L.M. Lei, X. Huang, M.M. Wang, L.Q. Wang, J.N. Qin, S.Q. Lu, Effect of temperature on deformation behavior and microstructures of TC11 titanium alloy, *Mater. Sci. Eng. A* 528 (2011) 8236–8243.
- [20] Y.B. Hao, Y.L. Huang, K. Zhao, C.Q. Qi, Y. Du, Research on the microstructure and mechanical properties of doubled annealed laser melting deposition TC11 titanium alloy, *Opt. Laser Technol.* 150 (2022) 107983.
- [21] Y.T. Liu, Y.Z. Zhang, Microstructure and mechanical properties of TA15-Ti2AlNb bimetallic structures by laser additive manufacturing, *Mater. Sci. Eng. A* 795 (2020) 140019.
- [22] H. Wang, S.Y. Ma, J.C. Wang, T. Lu, C.M. Liu, Microstructure and mechanical properties of TA15/TC11 graded structural material by wire arc additive manufacturing process, *Trans. Nonferrous Met. Soc. China* 31 (2021) 2323–2335.
- [23] H.S. Ren, D. Liu, H.B. Tang, X.J. Tian, Y.Y. Zhu, H.M. Wang, Microstructure and mechanical properties of a graded structural material, *Mater. Sci. Eng. A* 611 (2014) 362–369.
- [24] P.F. Jiang, X.R. Li, X.M. Zong, X.B. Wang, Z.K. Chen, H.X. Yang, C.Z. Liu, N.K. Gao, Z.H. Zhang, Multi-wire arc additive manufacturing of Ti basic heterogeneous alloy: Effect of deposition current on the microstructure, mechanical property and corrosion-resistance, *J. Alloy. Compd.* 920 (2022) 166056.
- [25] T.R. Anthony, H.E. Cline, Surface rippling induced by surface-tension gradients during laser surface melting and alloying, *J. Appl. Phys.* 3888 (48) (1977) 3888–3894.
- [26] X.B. Bai, P. Colegrove, J.L. Ding, X.M. Zhou, C.L. Diao, P. Bridgeman, J. roman Hönnige, H.O. Zhang, S. Williams, Numerical analysis of heat transfer and fluid

- flow in multilayer deposition of PAW-based wire and arc additive manufacturing, *Int. J. Heat. Mass Tran.* 124 (2018) 504–516.
- [27] P.F. Jiang, C.H. Zhang, S. Zhang, J.B. Zhang, J. Chen, H.T. Chen, Additive manufacturing of novel ferritic stainless steel by selective laser melting: Role of laser scanning speed on the formability, microstructure and properties, *Opt. Laser Technol.* 140 (2021) 107055.
- [28] P.F. Jiang, C.H. Zhang, S. Zhang, J.B. Zhang, J. Chen, Y. Liu, Microstructure evolution, wear behavior, and corrosion performance of alloy steel gradient material fabricated by direct laser deposition, *J. Mater. Res. Technol.* 9 (5) (2020) 11702–11716.
- [29] S. Cao, Rk Chu, X.G. Zhou, K. Yang, Q.B. Jia, C.V. Samuel Lim, A.J. Huang, X.H. Wu, Role of martensite decomposition in tensile properties of selective laser melted Ti-6Al-4V, *J. Alloy. Compd.* 744 (2018) 357–363.
- [30] E. Sallica-Leva, R. Caram, A.L. Jardini, J.B. Fogagnolo, Ductility improvement due to martensite α decomposition in porous Ti-6Al-4V parts produced by selective laser melting for orthopedic implants, *J. Mech. Behav. Biomed.* 54 (2016) 149–158.
- [31] Ln Xue, J.F. Xiao, Z.H. Nie, F. Hao, R. Chen, C.M. Liu, X.D. Yu, C.W. Tan, Dynamic response of Ti-6.5Al-1Mo-1V-2Zr-0.1B alloy fabricated by wire arc additive manufacturing, *Mater. Sci. Eng. A* 800 (2021) 140310.
- [32] X.Z. Shi, S.Y. Ma, C.M. Liu, Q.R. Wu, J.P. Lu, Y.D. Liu, W.T. Shi, Selective laser melting-wire arc additive manufacturing hybrid fabrication of Ti-6Al-4V alloy: Microstructure and mechanical properties, *Mater. Sci. Eng. A* 684 (2017) 196–204.
- [33] Z.X. Li, C.M. Liu, T.Q. Xu, L. Ji, D.H. Wang, J.P. Lu, S.Y. Ma, H.L. Fan, Reducing arc heat input and obtaining equiaxed grains by hot-wire method during arc additive manufacturing titanium alloy, *Mater. Sci. Eng. A* 742 (2019) 287–294.
- [34] A.S. Gornakova, S.I. Prokofiev, K.I. Kolesnikova, B.B. Straumal, Formation Regularities of Grain-Boundary Interlayers of the α -Ti Phase in Binary Titanium Alloys, *Russ. J. Non-Ferr. Met.* 57 (2016) 229–235.
- [35] M. Meng, X.G. Fan, L.G. Guo, M. Zhan, Achieving fine-grained equiaxed alpha via thermo-mechanical loading under off-equilibrium state in two-phase Ti-alloys, *J. Mater. Process. Technol.* 259 (2018) 397–408.
- [36] W.A. Soffa, David E. Laughlin, *Diffus. Phase Transform. Solid State* (2014).
- [37] M. Meng, H. Yang, X.G. Fan, S.L. Yan, A.M. Zhao, S. Zhu, On the modeling of diffusion-controlled growth of primary alpha in heat treatment of two-phase Ti-alloys, *J. Alloy. Compd.* 691 (2017) 67–80.
- [38] X.G. Fan, H. Yang, S.L. Yan, P.F. Gao, J.H. Zhou, Mechanism and kinetics of static globularization in TA15 titanium alloy with transformed structure, *J. Alloy. Compd.* 533 (2012) 1–8.
- [39] C.K. Syn, D.R. Lesuer, O.D. Sherby, Enhancing tensile ductility of a particulate-reinforced aluminum metal matrix composite by lamination with Mg-9%Li alloy, *Mater. Sci. Eng. A* 206 (1996) 201–207.
- [40] J.C. Wang, Y.J. Liu, S.X. Liang, Y.S. Zhang, L.Q. Wang, T.B. Sercombe, L.C. Zhang, Comparison of microstructure and mechanical behavior of Ti-35Nb manufactured by laser powder bed fusion from elemental powder mixture and prealloyed powder, *J. Mater. Sci. Technol.* 105 (2022) 1–16.
- [41] C.C. Jing, Z. Chen, B. Liu, T.Q. Xu, J. Wang, T. Lu, J.P. Lu, Y.L. Guo, C.M. Liu, Improving mechanical strength and isotropy for wire-arc additive manufactured 304L stainless steels via controlling arc heat input, *Mater. Sci. Eng. A* 845 (2022) 143223.
- [42] X.Y. Zhang, W.J. Jia, X.N. Mao, Effect of microstructure on the tensile properties and impact toughness of TC21G titanium alloy, *Mater. Char.* 185 (2022) 111752.
- [43] X. Cui, S. Zhang, Z.Y. Wang, C.H. Zhang, C.L. Ni, C.L. Wu, Microstructure and fatigue behavior of 24CrNiMo low alloy steel prepared by selective laser melting, *Mater. Sci. Eng. A* 845 (2022) 143215.